Article:
Chen, L, Sun, K, Shalashilin, DV et al. (2021) Efficient simulation of time- and frequency-resolved four-wave-mixing signals with a multiconfigurational Ehrenfest approach. The Journal of Chemical Physics, 154 (5). 054105. ISSN: 0021-9606

https://doi.org/10.1063/5.0038824

Efficient simulation of time- and frequency-resolved four-wave-mixing signals with Multiconfigurational Ehrenfest approach

Lipeng Chen[1], Kewei Sun[2], Dmitrii V. Shalashilin[3], Maxim F. Gelin[2] [a], Yang Zhao [4] [b]

[1] *Max Planck Institute for the Physics of Complex Systems, Nöthnitzer Str 38, Dresden, Germany*

[2] *School of Science, Hangzhou Dianzi University, Hangzhou 310018, China*

[3] *School of Chemistry, University of Leeds, Leeds LS2 9JT, United Kingdom*

[4] *Division of Materials Science, Nanyang Technological University, Singapore 639798, Singapore*

Abstract

We have extended the multiconfigurational Ehrenfest (MCE) approach to the simulation of four-wave-mixing signals of systems involving multiple electronic and vibrational degrees of freedom. As an illustration, we calculate the signals of three widely used spectroscopic techniques, time and frequency-resolved fluorescence spectroscopy, transient absorption spectroscopy, and two-dimensional (2D) electronic spectroscopy, for a two-electronic-state, twenty-four vibrational-mode conical intersection model. It has been shown that all three spectroscopic signals characterize the fast population transfer from the higher excited electronic state to the lower excited electronic state. While the time and frequency-resolved spectrum maps the wave packet propagation exclusively on the electronic excited states, the transient absorption and 2D electronic spectra reflect the wave-packet dynamics on both electronic excited states and electronic ground state. Combining the trajectory-guided Gaussian basis functions and the nonlinear response function formalism, the present approach thus provides a promising general technique for the applications of various Gaussian basis methods to the calculations of four-wave-mixing spectra of polyatomic molecules.

[a] Electronic address: maxim@hdu.edu.cn

[b] Electronic address: YZhao@ntu.edu.sg

I. INTRODUCTION

Modern techniques of nonlinear femtosecond spectroscopy have largely reshaped our understanding of photoinduced dynamic processes in chemical physics [1, 2]. Femtosecond spectroscopic signals, representing nonlinear responses of a materials system under study to external laser fields, are detected as functions of interpulse time delays and/or pulse carrier frequencies. In so-called four-wave-mixing (4WM) experiments, three coherent laser pulses are incident on the system, the response of which is measured in a given phase-matched direction. These 4WM spectroscopies include, among others, coherent anti-Stokes Raman spectroscopy, transient-grating spectroscopy, photon-echo spectroscopy [2]. In particular, with much success, two dimensional (2D) electronic spectroscopy has emerged as a powerful technique to scrutinize the intricate interplay between electronic and vibrational degrees of freedom (DOFs) in biological systems [3–5]. However, the interpretation of these signals in terms of dynamic processes in molecular systems is not straightforward. To decipher the information encoded in the spectroscopic signals, one has to solve coupled electronic and nuclear dynamics, an increasingly challenging task as the DOFs expand.

The information coded in the 4WM signals is uniquely characterized by the third-order polarization, which is in turn determined by nonlinear response functions and properties of the laser pulses involved [2]. For simple materials systems, such as harmonic oscillators or few-level systems, the response functions can be calculated either by the sum-over-states method or analytically by the cumulant expansion technique, while for complex materials systems, the evaluation of the multi-time response functions necessitates numerical methods capable of treating coupled electronic-vibrational dynamics in a sufficiently accurate and efficient manner [6–8]. There exist two alternative groups of theoretical methods for simulating many-body quantum dynamics in molecular systems. The methods of the first group are based on system-bath partitioning and treating the effect of vibrational modes as a thermal bath of harmonic oscillators. One then obtains the equations of motion for the reduced density matrix of the system, also referred to as quantum master equations (QMEs) [9], by taking into account the bath-induced relaxation and dissipation via the bath correlation function. Typical examples of QMEs approaches range from the second-order perturbative Redfield equation [10], approximate QMEs methods based on a polaron transformation [11, 12], to numerically exact hierarchical equations of motion (HEOM) [13, 14] and methods

of quasi-adiabatic propagator path integral [15]. While QMEs methods have been widely used to simulate dissipative quantum dynamics of complex systems, their applicability is restricted to certain forms of system-bath Hamiltonians and dynamics of vibrational DOFs cannot be handled explicitly by QMEs. An alternative to the QMEs approaches is the wave function methods, in which the wave function is expanded in a set of basis functions for both electronic and vibrational DOFs. One of the most popular, powerful wave function-based approaches is the multiconfiguration time-dependent Hartree (MCTDH) method [16, 17] and its multilayer extension (ML-MCTDH) [18, 19], which provides highly efficient tools for propagating wave packets with many DOFs at low temperatures.

One particularly promising technique for accurate simulation of quantum dynamics of complex molecular systems is the so-called Gaussian basis methods which employ time-dependent Gaussian basis functions [20]. Since an arbitrary nuclear wave function can be expanded as a linear combination of time-dependent coherent states, the Gaussian basis methods can in principle achieve a formally exact description of quantum dynamics once the Gaussian basis is sufficiently expanded toward completeness. Typical approaches using time-dependent Gaussian basis functions include the multiple spawning (MS) method [21, 22], the coupled coherent states (CCS) [23, 24], the multiconfigurational Ehrenfest (MCE) method [25, 26], the methods of variational Multiconfigurational Gaussians (vMCG) [27], the hierarchy of the Davydov ansätze (DA) [28–33], and the Gaussian-based multiconfiguration time-dependent Hartree (G-MCTDH) method [34]. It has been shown that the Gaussian basis method with the center of each Gaussian moving along the classical trajectory already yields accurate spectra of time-resolved stimulated emission in molecular systems if sufficient Gaussians are included [35]. The MS method has been extended to introduce an external field to drive the combined electronic-nuclear dynamics in photo-excited molecules triggered by atto- and femtosecond laser pulses [36]. The CCS method has been applied to simulate the high-order harmonic generation spectra of an electron in strong laser fields, yielding results in good agreement with exact calculations [37]. By integrating the DA into the framework of nonlinear response functions, one can calculate the four-wave-mixing signals of molecular aggregates with both singly and doubly excited electronic states taken into account [38, 39]. The G-MCTDH method was recently used to evaluate the time-resolved coherent Raman spectra of the embedded I_2Kr_{18}, offering a valuable tool to map calculated signals to wave packet coherence [40]. Very recently, a single-trajectory semiclassical thawed

Gaussian approximation has been applied for the evaluation of third-order response functions [41].

Previously, it has been demonstrated that the absorption spectrum of the S_2/S_1 pyrazine model can be efficiently and accurately computed by the MCE approach with a small number of trajectory-guided Gaussian basis functions [42]. In this paper, an efficient numerical scheme for the calculation of four-wave-mixing signals is developed by integrating the MCE method into the third-order nonlinear response functions formalism. The rest of the paper is organized as follows. In Sec. II we describe the model Hamiltonian, the MCE method, and the essential theoretical concepts of four-wave-mixing signals. In Sec. III, the application of the developed method to the pyrazine model is shown and discussed. Conclusions are drawn in Sec. IV.

II. THEORY

A. The model Hamiltonian

We consider a linear vibronic coupling model of pyrazine, which includes an electronic ground state $|g\rangle$, and two lowest excited electronic states $|S_1\rangle$ $(n\pi^*)$ and $|S_2\rangle$ $(\pi\pi^*)$ [43, 44]. Let H_g denote the electronic ground state Hamiltonian and H_e denote the electronic excited state Hamiltonian. Then the molecular system Hamiltonian H_S can be written as a sum of H_g and H_e

$$H_S = H_g + H_e \tag{1}$$

with

$$H_g = |g\rangle h_g \langle g|, \tag{2}$$

$$H_e = \sum_{k}^{S_1,S_2} |k\rangle \left(h_k + \epsilon_k\right) \langle k| + \sum_{k\neq k'}^{S_1,S_2} |k\rangle V_{kk'} \langle k'| \tag{3}$$

Here ϵ_k, $k = S_1, S_2$, is the vertical excitation energy of the kth excited state. h_g and h_k are vibrational Hamiltonians of the corresponding electronic ground state and kth excited electronic state, while $V_{kk'}$ is the interstate vibrational Hamiltonian. Keeping only the linear

Table I. Vertical excitation energies ϵ (eV), intrastate electron-vibrational coupling constants κ (eV), interstate electronic coupling constant λ (eV), vibrational frequencies ω (eV) and periods $\tau = 2\pi/\omega$ (fs).

	$S_1(n\pi^*)$	$S_2(\pi\pi^*)$	ω	$\tau = 2\pi/\omega$
ϵ	3.9283	4.8517		
κ_{6a}	-0.0964	0.1194	0.0740	55.9
κ_1	0.0470	0.2012	0.1273	32.5
κ_{9a}	0.1594	0.0484	0.1568	26.3
κ_{10a}	0	0	0.0936	44.2
		$\lambda = 0.1825$		

vibronic-coupling terms, the vibrational Hamiltonians read

$$h_g = \sum_{l=10a,6a,1,9a} \frac{\omega_l}{2}\left(-\frac{\partial^2}{\partial Q_l^2} + Q_l^2\right), \tag{4}$$

$$h_k = h_g + \sum_{m=6a,1,9a} \kappa_m^k Q_m, \tag{5}$$

$$V_{kk'} = \lambda Q_{10a}, \tag{6}$$

where Q_l is the dimensionless coordinate of the lth normal mode (labeled as $l = 1, 6a, 9a, 10a$) with frequency ω_l. The tuning modes (labeled as $m = 6a, 1, 9a$) have the intra-state electron-vibrational coupling constants κ_m^k ($k = S_1, S_2$), and the normal mode v_{10a} is the only coupling mode which connects two excited electronic states with an inter-state coupling constant λ. Various parameters of the system Hamiltonian are listed in Table I. Fig. 1 shows the one-dimensional cuts of resulting adiabatic potential energy surfaces (PESs) along the four system modes Q_1, Q_{6a}, Q_{9a}, and Q_{10a}.

The remaining weakly coupled vibrational modes can be considered as a heat bath, which consists of 20 harmonic oscillators [43, 44]

$$H_B = \sum_{n=1}^{20} \frac{\omega_n}{2}\left(-\frac{\partial^2}{\partial Q_n^2} + Q_n^2\right) \tag{7}$$

The system-bath coupling Hamiltonian is set to be diagonal in the electronic manifold

$$H_{\mathrm{SB}} = \sum_{n=1}^{20} \sum_{k=\mathrm{S}_1,\mathrm{S}_2} |k\rangle\langle k| \kappa_n^k Q_n, \tag{8}$$

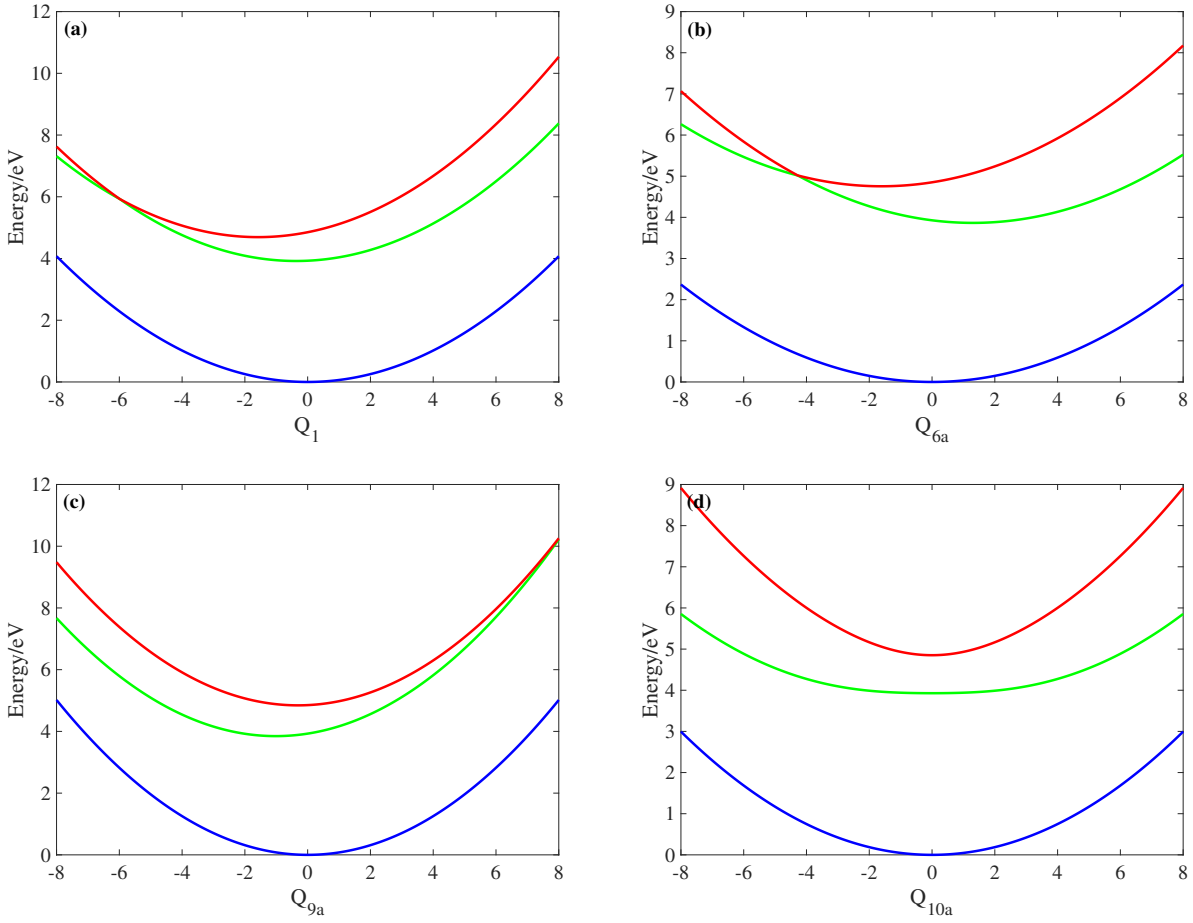

Figure 1. One-dimensional cuts of adiabatic PESs of the electronic ground state (blue), S_1 state (green), and S_2 state (red) along the dimensional normal modes Q_1 (a), Q_{6a} (b), Q_{9a} (c), and Q_{10a} (d).

where κ_n^k denote the linear electron-vibrational coupling constants for bath modes. The values of the vibrational frequencies and linear electronic-vibrational coupling constants for bath modes can be found in Table I of Ref. [44].

Finally, the total Hamiltonian is thus a sum of the system Hamiltonian H_S, the bath Hamiltonian H_B, and the system-bath coupling Hamiltonian H_{SB}

$$H = H_S + H_B + H_{SB} \tag{9}$$

B. The multiconfigurational Ehrenfest method

We first use the creation and annihilation operators to rearrange Eqs. (1)-(8) in a compact form

$$H = \sum_{k=\mathrm{S}_1,\mathrm{S}_2} \epsilon_k |k\rangle\langle k| + \sum_q \omega_q b_q^\dagger b_q + \frac{1}{\sqrt{2}} \sum_{k\neq k'}^{\mathrm{S}_1,\mathrm{S}_2} \lambda |k\rangle\langle k'| \left(b_{10a}^\dagger + b_{10a}\right) + \frac{1}{\sqrt{2}} \sum_{k=\mathrm{S}_1,\mathrm{S}_2} \sum_{q\neq 10a} \kappa_q^k |k\rangle\langle k| \left(b_q^\dagger + b_q\right) \tag{10}$$

where q labels 4 primary system modes plus 20 bath modes, $b_q^\dagger(b_q)$ is the creation (annihilation) operator of the qth mode.

To solve the time-dependent Schrödinger equation, we adopt the MCE method in which the wave function is constructed as a superposition of M configurations

$$\begin{aligned} |\Psi(t)\rangle =& \sum_{u=1}^{M} \left(\sum_k^{\mathrm{S}_1,\mathrm{S}_2} A_{uk}(t)|k\rangle \right) |\mathbf{z}_u(t)\rangle \\ =& \sum_{u=1}^{M} \left(\sum_k^{\mathrm{S}_1,\mathrm{S}_2} A_{uk}(t)|k\rangle \right) \exp\left[\sum_q \left(z_{uq} b_q^\dagger - z_{uq}^* b_q \right) \right] |0\rangle_{\mathrm{ph}} \end{aligned} \tag{11}$$

where u is the configuration index. A_{uk} is the amplitude in the diabatic state $|k\rangle$, and z_{uq} represent the phonon displacements.

In order to derive the equations of motion for wave function parameters A_{uk} and $\mathbf{z}_u$, we first formulate the Lagrangian L as

$$\begin{aligned} L =& \langle\Psi(t)| i\frac{\partial}{\partial t} - H|\Psi(t)\rangle \\ =& \frac{i}{2} \sum_{nu}^{M} \sum_k^{\mathrm{S}_1,\mathrm{S}_2} \left\{ \left[A_{nk}^* \dot{A}_{uk} - \dot{A}_{nk}^* A_{uk} \right] + A_{nk}^* A_{uk} \sum_q \left(\frac{z_{nq}\dot{z}_{nq}^* + \dot{z}_{nq} z_{nq}^* - z_{uq}\dot{z}_{uq}^* - \dot{z}_{uq} z_{uq}^*}{2} + z_{nq}^* \dot{z}_{uq} - \dot{z}_{nq}^* z_{uq} \right) \right\} \\ & \times R_{nu} - \langle\Psi(t)|H|\Psi(t)\rangle \end{aligned} \tag{12}$$

where

$$R_{nu} = \langle \mathbf{z}_n | \mathbf{z}_u \rangle = \exp\left\{ \sum_q z_{nq}^* z_{uq} - \frac{1}{2} \left(|z_{nq}|^2 + |z_{uq}|^2 \right) \right\} \tag{13}$$

and

$$\begin{aligned} & \langle\Psi(t)|H|\Psi(t)\rangle \\ =& \sum_{nu}^{M} \left\{ A_{n\mathrm{S}_1}^* A_{u\mathrm{S}_1} \left[\epsilon_{\mathrm{S}_1} + \sum_q \omega_q z_{nq}^* z_{uq} + \sum_q \frac{\kappa_q^{\mathrm{S}_1}}{\sqrt{2}} \left(z_{nq}^* + z_{uq} \right) \right] + A_{n\mathrm{S}_1}^* A_{u\mathrm{S}_2} \sum_q \frac{\lambda_q}{\sqrt{2}} \left(z_{nq}^* + z_{uq} \right) \right\} R_{nu} \\ & + \sum_{nu}^{M} \left\{ A_{n\mathrm{S}_2}^* A_{u\mathrm{S}_2} \left[\epsilon_{\mathrm{S}_2} + \sum_q \omega_q z_{nq}^* z_{uq} + \sum_q \frac{\kappa_q^{\mathrm{S}_2}}{\sqrt{2}} \left(z_{nq}^* + z_{uq} \right) \right] + A_{n\mathrm{S}_2}^* A_{u\mathrm{S}_1} \sum_q \frac{\lambda_q}{\sqrt{2}} \left(z_{nq}^* + z_{uq} \right) \right\} R_{nu} \end{aligned} \tag{14}$$

The equations of motion for $A_{n\mathrm{S}_1}$ and $A_{n\mathrm{S}_2}$ can be obtained from the Euler equations

$$-\frac{d}{dt}\left[\frac{\partial L}{\partial \dot{A}^*_{u\mathrm{S}_1}}\right]+\frac{\partial L}{\partial A^*_{u\mathrm{S}_1}}=0, \tag{15}$$

$$-\frac{d}{dt}\left[\frac{\partial L}{\partial \dot{A}^*_{u\mathrm{S}_2}}\right]+\frac{\partial L}{\partial A^*_{u\mathrm{S}_2}}=0. \tag{16}$$

yielding

$$\begin{aligned}
&i\sum_n^M\left\{\dot{A}_{n\mathrm{S}_1}+A_{n\mathrm{S}_1}\sum_q\left[z^*_{mq}\dot{z}_{nq}-\frac{\dot{z}_{nq}z^*_{nq}+z_{nq}\dot{z}^*_{nq}}{2}\right]\right\}R_{mn}\\
=&\sum_n^M\left\{A_{n\mathrm{S}_1}\left[\epsilon_{\mathrm{S}_1}+\sum_q\omega_q z^*_{mq}z_{nq}+\sum_q\frac{\kappa_q^{S_1}}{\sqrt{2}}\left(z^*_{mq}+z_{nq}\right)\right]+A_{n\mathrm{S}_2}\sum_q\frac{\lambda_q}{\sqrt{2}}\left(z^*_{mq}+z_{nq}\right)\right\}R_{mn},
\end{aligned} \tag{17}$$

$$\begin{aligned}
&i\sum_n^M\left\{\dot{A}_{n\mathrm{S}_2}+A_{n\mathrm{S}_2}\sum_q\left[z^*_{mq}\dot{z}_{nq}-\frac{\dot{z}_{nq}z^*_{nq}+z_{nq}\dot{z}^*_{nq}}{2}\right]\right\}R_{mn}\\
=&\sum_n^M\left\{A_{n\mathrm{S}_2}\left[\epsilon_{\mathrm{S}_2}+\sum_q\omega_q z^*_{mq}z_{nq}+\sum_q\frac{\kappa_q^{S_2}}{\sqrt{2}}\left(z^*_{mq}+z_{nq}\right)\right]+A_{n\mathrm{S}_1}\sum_q\frac{\lambda_q}{\sqrt{2}}\left(z^*_{mq}+z_{nq}\right)\right\}R_{mn}.
\end{aligned} \tag{18}$$

The equation of motion for $\mathbf{z}_n$ is obtained by considering that each $\mathbf{z}_n$ follows its own Ehrenfest trajectory, i.e.,

$$\begin{aligned}
i\dot{\mathbf{z}}_n&=\frac{\partial H_n^{\mathrm{Ehr}}}{\partial \mathbf{z}_n^*},\\
H_n^{\mathrm{Ehr}}&=\frac{\langle\Psi_n|H|\Psi_n\rangle}{\langle\Psi_n|\Psi_n\rangle},\\
|\Psi_n\rangle&=\left(A_{n\mathrm{S}_1}|\mathrm{S}_1\rangle+A_{n\mathrm{S}_2}|\mathrm{S}_2\rangle\right)|\mathbf{z}_n\rangle
\end{aligned} \tag{19}$$

where

$$\begin{aligned}
&\langle\Psi_n|H|\Psi_n\rangle\\
=&A^*_{n\mathrm{S}_1}A_{n\mathrm{S}_1}\left[\epsilon_{\mathrm{S}_1}+\sum_q\omega_q z^*_{nq}z_{nq}+\sum_q\frac{\kappa_q^{S_1}}{\sqrt{2}}\left(z^*_{nq}+z_{nq}\right)\right]+A^*_{n\mathrm{S}_1}A_{n\mathrm{S}_2}\sum_q\frac{\lambda_q}{\sqrt{2}}\left(z^*_{nq}+z_{nq}\right)\\
&+A^*_{n\mathrm{S}_2}A_{n\mathrm{S}_2}\left[\epsilon_{\mathrm{S}_2}+\sum_q\omega_q z^*_{nq}z_{nq}+\sum_q\frac{\kappa_q^{S_2}}{\sqrt{2}}\left(z^*_{nq}+z_{nq}\right)\right]+A^*_{n\mathrm{S}_2}A_{n\mathrm{S}_1}\sum_q\frac{\lambda_q}{\sqrt{2}}\left(z^*_{nq}+z_{nq}\right)
\end{aligned} \tag{20}$$

and

$$\langle\Psi_n|\Psi_n\rangle = A^*_{n\mathrm{S}_1}A_{n\mathrm{S}_1} + A^*_{n\mathrm{S}_2}A_{n\mathrm{S}_2} \tag{21}$$

One thus arrives at the equation of motion for z_{nq}

$$i\dot{z}_{nq} = \frac{A^*_{n\mathrm{S}_1}A_{n\mathrm{S}_1}\left(\omega_q z_{nq} + \frac{\kappa_q^{S_1}}{\sqrt{2}}\right) + A^*_{n\mathrm{S}_1}A_{n\mathrm{S}_2}\frac{\lambda_q}{\sqrt{2}} + A^*_{n\mathrm{S}_2}A_{n\mathrm{S}_2}\left(\omega_q z_{nq} + \frac{\kappa_q^{S_2}}{\sqrt{2}}\right) + A^*_{n\mathrm{S}_2}A_{n\mathrm{S}_1}\frac{\lambda_q}{\sqrt{2}}}{A^*_{n\mathrm{S}_1}A_{n\mathrm{S}_1} + A^*_{n\mathrm{S}_2}A_{n\mathrm{S}_2}} \tag{22}$$

In our simulations, the quantum superposition sampling [45] is used to obtain the amplitudes of the diabatic states A_{uk}, and the phonon displacements z_{uq} (both the real and the imaginary part) are sampled from a uniformly distributed noise within the range $[-\delta, \delta]$ (δ=5 $\times$ 10^{-2} for the system modes and δ = 10^{-2} for the bath modes, respectively). A configuration of $M = 800$ is employed to achieve converged results.

C. Third-order response functions

To simulate 4WM signals, one needs to evaluate the response of the system on three laser fields. The system-field interaction Hamiltonian is defined in the rotating wave approximation as

$$H_L = -\sum_{\alpha=1}^{3}\left(\mathbf{E}_\alpha(\mathbf{r},t)\cdot\boldsymbol{\mu}_+ + \mathbf{E}^*_\alpha(\mathbf{r},t)\cdot\boldsymbol{\mu}_-\right) \tag{23}$$

Here, vectors are denoted in boldface. $\boldsymbol{\mu}_+$ and $\boldsymbol{\mu}_-$ are the up and down transition dipole moment operators and

$$\mathbf{E}_\alpha(\mathbf{r},t) = \mathbf{e}_\alpha E_\alpha(t-\tau_\alpha)e^{i\mathbf{k}_\alpha\cdot\mathbf{r}-i\omega_\alpha t} \tag{24}$$

where $\mathbf{e}_\alpha$, $E_\alpha(t)$, τ_α, $\mathbf{k}_\alpha$, ω_α are the polarization, dimensionless envelope, central time, wave vector, and the frequency of the αth laser pulse, respectively. In a typical 4WM experiment, the central times of the first three laser pulses are defined as

$$\tau_1 = -T_\mathrm{w} - \tau, \quad \tau_2 = -T_\mathrm{w}, \quad \tau_3 = 0, \tag{25}$$

Here, τ is the time delay between the second and the first laser pulses, and T_w (the so-called population time) is the time delay between the third and the second laser pulses.

Next we need to evaluate four third-order response functions R_a, $a = 1, 2, 3, 4$, which are in turn calculated by the four-time correlation function of the transition dipole moment

operators as [1]

$$R_1(t_3,t_2,t_1) = \Phi(t_1, t_1+t_2, t_1+t_2+t_3, 0), \tag{26}$$

$$R_2(t_3,t_2,t_1) = \Phi(0, t_1+t_2, t_1+t_2+t_3, t_1), \tag{27}$$

$$R_3(t_3,t_2,t_1) = \Phi(0, t_1, t_1+t_2+t_3, t_1+t_2), \tag{28}$$

$$R_4(t_3,t_2,t_1) = \Phi(t_1+t_2+t_3, t_1+t_2, t_1, 0). \tag{29}$$

The four-time correlation function at zero temperature limit can be further simplified as [38, 39, 46]

$$\Phi(\tau_4,\tau_3,\tau_2,\tau_1) = \langle\Phi_0|\mu_- e^{-\frac{i}{\hbar}H(\tau_4-\tau_3)}\mu_+ e^{-\frac{i}{\hbar}H_{\rm ph}(\tau_3-\tau_2)}\mu_- e^{-\frac{i}{\hbar}H(\tau_2-\tau_1)}\mu_+|\Psi_0\rangle, \tag{30}$$

Here, $H_{\rm ph} = \sum_q \omega_q b_q^\dagger b_q$, and $|\Psi_0\rangle = |g\rangle|0\rangle_{\rm ph}$ denotes the initial state before photoexcitation, which is the vibrational ground state of the electronic ground state. The up and down transition dipole moment operators are defined as $\mu_+ = \mu_{\rm S_1}|{\rm S_1}\rangle\langle g| + \mu_{\rm S_2}|{\rm S_2}\rangle\langle g|$ and $\mu_- = \mu_+^\dagger$. The value of $\mu_{\rm S_1}$ and $\mu_{\rm S_2}$ are set to 0.0478 and 0.177, respectively [47]. By substituting MCE wave function of Eq. (11) into Eq. (30), one obtains the expressions for the four response functions R_a, $a = 1,2,3,4$ as follows

$$\begin{aligned}
R_1(\tau,T_{\rm w},t) =& \sum_{nu}^{M}\sum_{k,k_1,k_2,k_3} \left(\mathbf{e}_4^*\cdot\boldsymbol{\mu}_{k_2}^*\right)\left(\mathbf{e}_1\cdot\boldsymbol{\mu}_{k_3}\right)\left(\mathbf{e}_2^*\cdot\boldsymbol{\mu}_k^*\right)\left(\mathbf{e}_3\cdot\boldsymbol{\mu}_{k_1}\right) A_{nk_1}^{k*}(T_{\rm w}) A_{uk_2}^{k_3}(\tau+T_{\rm w}+t) \\
&\times \exp\left\{\sum_q z_{nq}^{k*}(T_{\rm w}) z_{uq}^{k_3}(\tau+T_{\rm w}+t) e^{i\omega_q t}\right\} e^{-\frac{1}{2}\sum_q\left(|z_{nq}^k(T_{\rm w})|^2+|z_{uq}^{k_3}(\tau+T_{\rm w}+t)|^2\right)} \\
R_2(\tau,T_{\rm w},t) =& \sum_{nu}^{M}\sum_{k,k_1,k_2,k_3} \left(\mathbf{e}_4^*\cdot\boldsymbol{\mu}_{k_2}^*\right)\left(\mathbf{e}_1^*\cdot\boldsymbol{\mu}_k^*\right)\left(\mathbf{e}_2\cdot\boldsymbol{\mu}_{k_3}\right)\left(\mathbf{e}_3\cdot\boldsymbol{\mu}_{k_1}\right) A_{nk_1}^{k*}(\tau+T_{\rm w}) A_{uk_2}^{k_3}(t+T_{\rm w}) \\
&\times \exp\left\{\sum_q z_{nq}^{k*}(\tau+T_{\rm w}) z_{uq}^{k_3}(t+T_{\rm w}) e^{i\omega_q t}\right\} e^{-\frac{1}{2}\sum_q\left(|z_{nq}^k(\tau+T_{\rm w})|^2+|z_{uq}^{k_3}(t+T_{\rm w})|^2\right)} \\
R_3(\tau,T_{\rm w},t) =& \sum_{nu}^{M}\sum_{k,k_1,k_2,k_3} \left(\mathbf{e}_4^*\cdot\boldsymbol{\mu}_{k_2}^*\right)\left(\mathbf{e}_1^*\cdot\boldsymbol{\mu}_k^*\right)\left(\mathbf{e}_2\cdot\boldsymbol{\mu}_{k_1}\right)\left(\mathbf{e}_3\cdot\boldsymbol{\mu}_{k_3}\right) A_{nk_1}^{k*}(\tau) A_{uk_2}^{k_3}(t) \\
&\times \exp\left\{\sum_q z_{nq}^{k*}(\tau) z_{uq}^{k_3}(t) e^{i\omega_q(T_{\rm w}+t)}\right\} e^{-\frac{1}{2}\sum_q\left(|z_{nq}^k(\tau)|^2+|z_{uq}^{k_3}(t)|^2\right)} \\
R_4(\tau,T_{\rm w},t) =& \sum_{nu}^{M}\sum_{k,k_1,k_2,k_3} \left(\mathbf{e}_4^*\cdot\boldsymbol{\mu}_k^*\right)\left(\mathbf{e}_1\cdot\boldsymbol{\mu}_{k_3}\right)\left(\mathbf{e}_2^*\cdot\boldsymbol{\mu}_{k_2}^*\right)\left(\mathbf{e}_3\cdot\boldsymbol{\mu}_{k_1}\right) A_{nk_1}^{k*}(-t) A_{uk_2}^{k_3}(\tau) \\
&\times \exp\left\{\sum_q z_{nq}^{k*}(-t) z_{uq}^{k_3}(\tau) e^{-i\omega_q T_{\rm w}}\right\} e^{-\frac{1}{2}\sum_q\left(|z_{nq}^k(-t)|^2+|z_{uq}^{k_3}(\tau)|^2\right)}
\end{aligned} \tag{31}$$

Here, $\mathbf{e}_4$ is the polarization of the local oscillator field, and $A^{k_3}_{uk_2}(t)$ denotes the probability amplitude of the electronic state $|k_2\rangle$ at time t given that the system resides in the electronic state $|k_3\rangle$ initially and with configuration u. $z^{k_3}_{uq}(t)$ is the corresponding phonon displacement at time t, also starting from $|k_3\rangle|0\rangle_{\rm ph}$. In the calculations, the response functions $R_a(\tau, \mathrm{T_w}, t), a = 1, 2, 3, 4$ (Eq. (31)) are further multiplied by $\exp\{-(\tau + t)/\tau_d\}$ with a dephasing time $\tau_d = 80$ fs in order to take into account additional optical dephasing, which is not described by the Hamiltonian of Eq. 10.

Since we only consider two lowest electronic excited states of pyrazine (higher excited electronic states are neglected in our model), the third-order polarization $P(\tau, \mathrm{T_w}, t)$ includes contributions from the stimulated emission (SE) and the ground state bleaching (GSB), each of which can be further decomposed into rephasing (superscript r) and nonrephasing (superscript nr) contributions

$$P_{\rm SE}(\tau, \mathrm{T_w}, t) = P^{(\rm r)}_{\rm SE}(\tau, \mathrm{T_w}, t) + P^{(\rm nr)}_{\rm SE}(\tau, \mathrm{T_w}, t), \tag{32}$$

$$P_{\rm GSB}(\tau, \mathrm{T_w}, t) = P^{(\rm r)}_{\rm GSB}(\tau, \mathrm{T_w}, t) + P^{(\rm nr)}_{\rm GSB}(\tau, \mathrm{T_w}, t). \tag{33}$$

In the ultrashort pulse approximation (the so-called impulsive limit), we have

$$\begin{aligned} P^{(\rm r)}_{\rm SE}(\tau, \mathrm{T_w}, t) &\sim -iR_2(\tau, \mathrm{T_w}, t), \\ P^{(\rm nr)}_{\rm SE}(\tau, \mathrm{T_w}, t) &\sim -iR_1(\tau, \mathrm{T_w}, t), \\ P^{(\rm r)}_{\rm GSB}(\tau, \mathrm{T_w}, t) &\sim -iR_3(\tau, \mathrm{T_w}, t), \\ P^{(\rm nr)}_{\rm GSB}(\tau, \mathrm{T_w}, t) &\sim -iR_4(\tau, \mathrm{T_w}, t). \end{aligned} \tag{34}$$

By performing two-dimensional Fourier transforms, one obtains

$$\begin{aligned} S^{(\rm r)}_{\rm SE}(\omega_\tau, \mathrm{T_w}, \omega_t) &= \mathrm{Re}\int_0^\infty d\tau dt i P^{(\rm r)}_{\rm SE}(\tau, \mathrm{T_w}, t) e^{-i\omega_\tau\tau + i\omega_t t}, \\ S^{(\rm nr)}_{\rm SE}(\omega_\tau, \mathrm{T_w}, \omega_t) &= \mathrm{Re}\int_0^\infty d\tau dt i P^{(\rm nr)}_{\rm SE}(\tau, \mathrm{T_w}, t) e^{i\omega_\tau\tau + i\omega_t t}, \\ S^{(\rm r)}_{\rm GSB}(\omega_\tau, \mathrm{T_w}, \omega_t) &= \mathrm{Re}\int_0^\infty d\tau dt i P^{(\rm r)}_{\rm GSB}(\tau, \mathrm{T_w}, t) e^{-i\omega_\tau\tau + i\omega_t t}, \\ S^{(\rm nr)}_{\rm GSB}(\omega_\tau, \mathrm{T_w}, \omega_t) &= \mathrm{Re}\int_0^\infty d\tau dt i P^{(\rm nr)}_{\rm GSB}(\tau, \mathrm{T_w}, t) e^{i\omega_\tau\tau + i\omega_t t}. \end{aligned} \tag{35}$$

The 2D electronic spectroscopy is a third-order photon-echo technique. The SE and GSB contributions to 2D spectra can be written as

$$S_{\rm SE}(\omega_\tau, \mathrm{T_w}, \omega_t) = S^{(\rm r)}_{\rm SE}(\omega_\tau, \mathrm{T_w}, \omega_t) + S^{(\rm nr)}_{\rm SE}(\omega_\tau, \mathrm{T_w}, \omega_t), \tag{36}$$

$$S_{\rm GSB}(\omega_\tau, \mathrm{T_w}, \omega_t) = S^{(\rm r)}_{\rm GSB}(\omega_\tau, \mathrm{T_w}, \omega_t) + S^{(\rm nr)}_{\rm GSB}(\omega_\tau, \mathrm{T_w}, \omega_t). \tag{37}$$

The total 2D spectrum is a sum of above two contributions

$$S(\omega_\tau, \mathrm{T_w}, \omega_t) = S_{\mathrm{SE}}(\omega_\tau, \mathrm{T_w}, \omega_t) + S_{\mathrm{GSB}}(\omega_\tau, \mathrm{T_w}, \omega_t). \tag{38}$$

The transient absorption (TA) spectroscopy is another popular 4WM technique, probing changes in the absorbance/transmittance of the system [2]. In a typical pump-probe experimental setup, the signal is measured in the probe laser direction. The TA polarization is evaluated by setting $\mathbf{k}_1 = \mathbf{k}_2 = \mathrm{k_{pump}}$ and $\mathbf{k}_3 = \mathbf{k}_{\mathrm{probe}}$, and in the impulsive limit, one has

$$P_{\mathrm{TA}}(\mathrm{T_w}, t) \sim -i\left[R_1(0, \mathrm{T_w}, t) + R_2(0, \mathrm{T_w}, t) + R_3(0, \mathrm{T_w}, t) + R_4(0, \mathrm{T_w}, t)\right] \tag{39}$$

The dispersed TA spectrum is defined as follows

$$S_{\mathrm{TA}}(\mathrm{T_w}, \omega_t) = \mathrm{Re}\int_0^\infty dt i P_{\mathrm{TA}}(\mathrm{T_w}, t) e^{i\omega_t t}. \tag{40}$$

The time and frequency-gated (TFG) fluorescence spectrum provides a detailed characterization of the excited state wave packet dynamics. It can be calculated as [48]

$$S_{\mathrm{TFG}}(\mathrm{T_w}, \omega_t) \sim \mathrm{Re}\int_0^\infty dt_2 dt R_2(0, t_2, t) e^{i\omega_t t} E_f(t + t_2 - \mathrm{T_w}) E_f(t_2 - \mathrm{T_w}) \tag{41}$$

Here, $E_f(t)$ is the envelop of the gate pulse, which is taken as Gaussian $E_f(t) = \exp\{-(t/\tau_f)^2\}$ with τ_f being the pulse duration. It should be noted that the time and frequency resolution of the signal is controlled by the gate pulse and the impulsive limit is not appropriate for the simulation of this signal.

III. RESULTS AND DISCUSSION

The TFG fluorescence spectroscopy monitors the wave packet movement of excited electronic states projected onto the electronic ground state of the system [48, 49]. We previously used the HEOM method to simulate the time and frequency-resolved fluorescence spectra of a two-state two-mode pyrazine model coupled to a dissipative environment, which demonstrates the close connection between the excited state wave packets and the time and frequency-resolved fluorescence spectra [50]. In Fig. 2, we display the TFG fluorescence spectra $S_{\mathrm{TFG}}(\mathrm{T_w}, \omega_t)$ of 24-mode pyrazine model for a good time resolution (a) and a good frequency resolution (b). The spectrum in the left panel reflects the vibronic wave packets of the excited $\mathrm{S_1}$ and $\mathrm{S_2}$ states. The signal is dominated by the emission from the $\mathrm{S_2}$ state

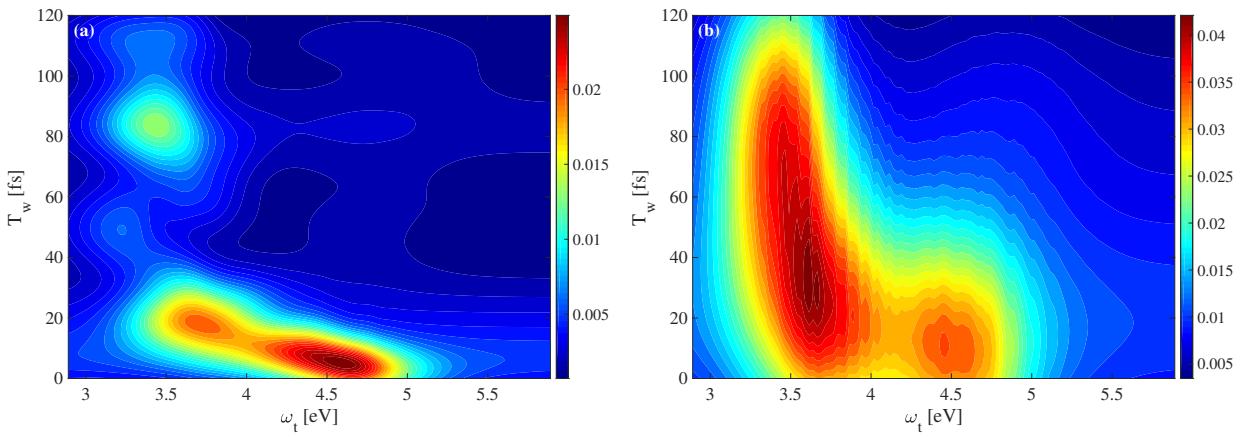

Figure 2. TFG fluorescence spectra $S_{\mathrm{TFG}}(\mathrm{T_w}, \omega_t)$ of 24-mode pyrazine model in the cases of (a) good time resolution (τ_f =12 fs) and (b) good frequency resolution (τ_f= 60 fs).

at short $\mathrm{T_w}$ due to a much larger transition dipole moment of the $\mathrm{S_2}$ state as compared to that of the $\mathrm{S_1}$ state. The emission from the $\mathrm{S_2}$ state gradually quenches as waiting time $\mathrm{T_w}$ increases, and one clearly observes the fast population transfer from the $\mathrm{S_2}$ state to the $\mathrm{S_1}$ state within $\sim$ 25 fs. However, this population transfer is not monotonous as can be seen from the recurrence of the $\mathrm{S_2}$ state emission at $\mathrm{T_w} \sim$ 85 fs, which is also consistent with the diabatic populations shown in Ref. [32]. As illustrated in Fig. 2(b), $S_{\mathrm{TFG}}(\mathrm{T_w}, \omega_t)$ calculated with a longer gate pulse (τ_f= 60 fs), on the other hand, exhibits a ridge pattern, which corresponds to emissions from the individual vibronic levels of the excited electronic states. Once again, the CI-driven fast population transfer from the $\mathrm{S_2}$ state to the $\mathrm{S_1}$ state is seen to occur within $\sim$ 25 fs, and the signal is dominated by the $\mathrm{S_1}$ emission after $\mathrm{T_w} >$ 60 fs. The TFG fluorescence spectra presented in Fig. 2 can be contrast with those of the 2-state 5-mode pyrazine model depicted in Ref. [51], which reveals that the addition of extra tuning modes accelerates the initial population transfer and suppresses the recurrence of the $\mathrm{S_2}$ state emission at later times.

In contrast to the TFG fluorescence spectra, the TA spectrum monitors the wave packet dynamics on both the electronic excited states and ground state. Fig. 3 plots the dispersed TA $S_{\mathrm{TA}}(\mathrm{T_w}, \omega_t)$ as a function of ω_t and time delay $\mathrm{T_w}$ between the pump and probe pulses. The TA spectrum includes contributions from the GSB and the SE. The GSB contribution is manifested as the strong ridge centred around 4.76 eV and several weak stripes in the range 3.69-4.09 eV. The former is originated from the $\mathrm{S_2}$ state, and the latter can be traced

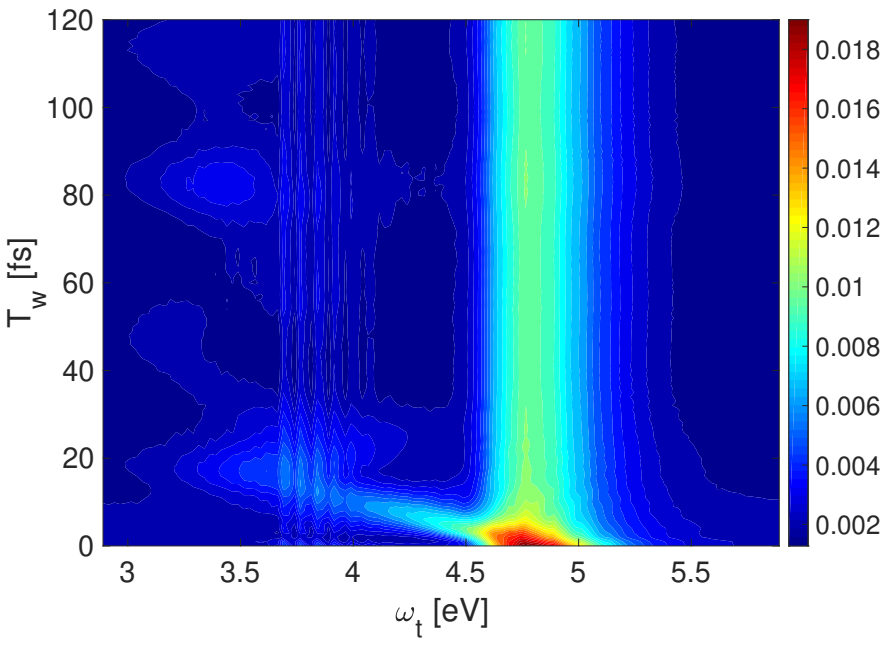

Figure 3. Dispersed transient absorption signal $S_{\mathrm{TA}}(\mathrm{T_w}, \omega_t)$ as a function of ω_t and time delay $\mathrm{T_w}$ between the pump and probe pulses.

back to the S_1 state. It is worth noting that the $\mathrm{T_w}$-dependent oscillations of the GSB contribution have small amplitudes, typical for the TA spectrum calculated in the short-pulse approximation [52]. The SE contribution features the fast population transfer from the S_2 state to the S_1 state within $\sim$ 25 fs, similar to the TFG fluorescence spectrum with a good time resolution. While the GSB and SE contributions coexist at longer delay time $\mathrm{T_w}$, the signal is dominated by the GSB contribution.

Electronic 2D spectroscopy is known to provide detailed information on the ultrafast relaxation process at conical intersections (CIs)[53–55]. Fig. 4 displays the 2D spectra $S(\omega_\tau, \mathrm{T_w}, \omega_t)$ of 24-mode pyrazine model at different population times $\mathrm{T_w}$. At $\mathrm{T_w} = 0$ fs, the spectra show pronounced vibronic multi-peak structure around $\omega_\tau = \omega_t = 4.765$ eV as well as much weaker diagonal peaks ranging from 3.69 eV to 4.09 eV, which correspond to the S_2 and S_1 bands in the absorption spectrum, respectively. Moreover, the S_2-S_1 and S_1-S_2 cross peaks are also pronounced . From $\mathrm{T_w} = 5$ fs to $\mathrm{T_w} = 25$ fs, one can clearly see the shift of the stimulated emission peaks along the ω_t axis to lower energies, which directly reflects the fact that the wave packet in the upper S_2 surface gradually approaches the CI and transfers to the lower S_1 surface. In addition, the intensity of S_1 diagonal peaks is also significantly decreased with $\mathrm{T_w}$. Due to the fast CI-driven S_2-S_1 population transfer, the

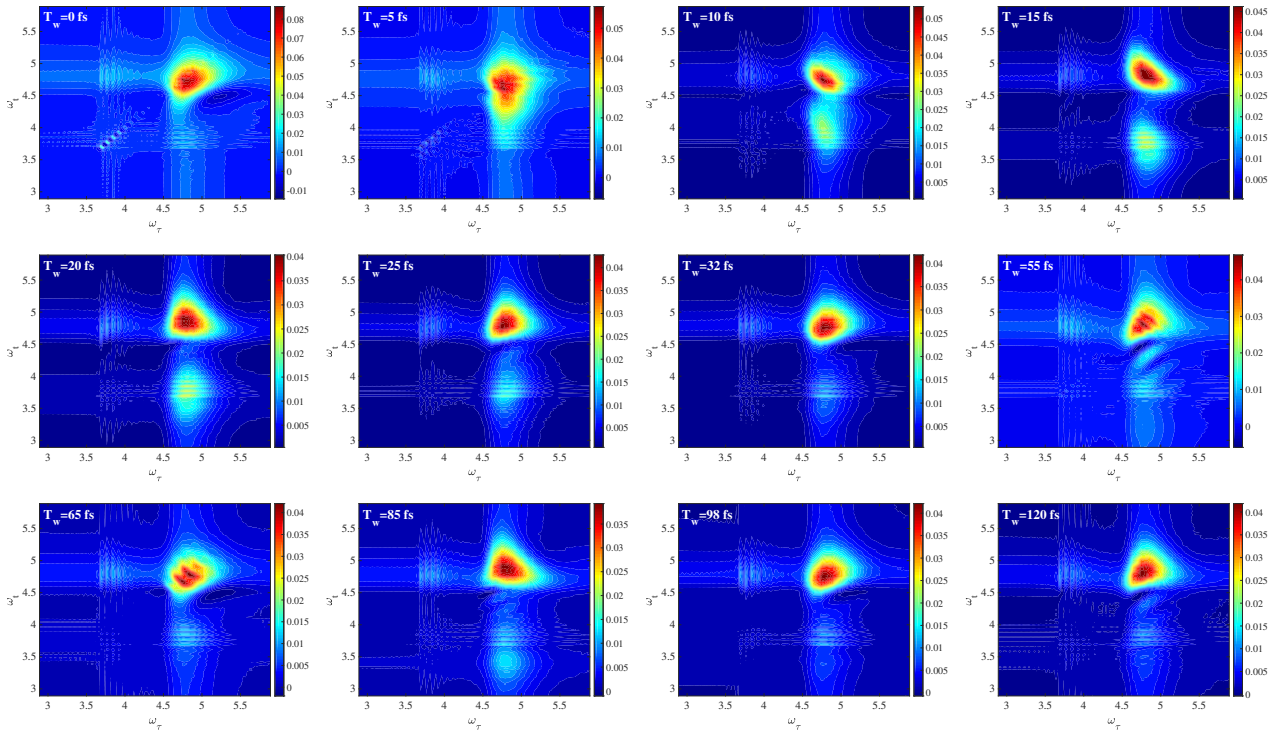

Figure 4. Real part of the total 2D electronic spectra $S(\omega_\tau, \mathrm{T_w}, \omega_t)$ of 24-mode pyrazine model for different population times $\mathrm{T_w}$.

overall intensity of the 2D spectrum at $\mathrm{T_w} = 25$ fs is roughly half of that at $\mathrm{T_w} = 0$ fs. At longer population time $\mathrm{T_w}$, the SE contribution becomes small and the total spectrum is dominated by the GSB contribution. The 2D spectra exhibit recurrence pattern as a function of $\mathrm{T_w}$ modulated by the tuning mode Q_1, which reflects the wave-packet evolution along the mode Q_1 in the electronic ground state. Since the vibrational period of mode Q_1 is 32.5 fs, $S(\omega_\tau, \mathrm{T_w}, \omega_t)$ evaluated at $\mathrm{T_w} = 32$, 65, and 98 fs look quite similar. It should be noted that the enhancement of the $\mathrm{S_2 - S_1}$ cross peaks at population time $\mathrm{T_w} = 85$ fs (due to the SE contribution) is consistent with those shown in the time-resolved fluorescence and TA spectra (see Figs. 2(a) and 3).

To retrieve the fine details of the evolution of 2D spectra, we also plot the $\mathrm{T_w}$-evolution of the intensities of two diagonal peaks (DPs) at ($\omega_\tau = \omega_t$ =4.64 eV) and ($\omega_\tau = \omega_t$ = 4.765 eV) and two cross peaks (CPs) at (ω_τ =4.64 eV, ω_t =4.765 eV) and (ω_τ =4.765 eV, ω_t =4.64 eV) in Fig. 5. Due to the fast decay of SE contribution, the amplitudes of both DPs and CPs decrease rapidly at short $\mathrm{T_w}$. The peak evolutions at longer $\mathrm{T_w}$ are dominated by the GSB contribution, which reflects the evolution of the ground state wave packet. The $\mathrm{T_w}$-evolution

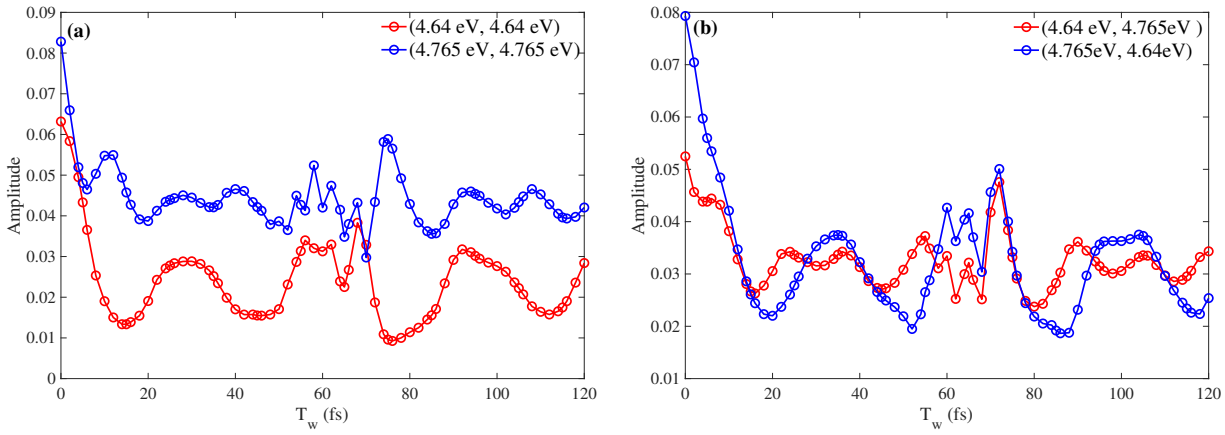

Figure 5. Amplitudes of the diagonal peaks (left panel, (ω_τ=4.64 eV, ω_t=4.64 eV), red and (ω_τ=4.765 eV, ω_t=4.765 eV), blue) and cross peaks (right panel, (ω_τ=4.64 eV, ω_t=4.765 eV), red and (ω_τ=4.765 eV, ω_t=4.64 eV), blue) as a function of population time T_w.

of both DPs and CPs exhibits irregular beating patterns, which cannot be assigned to the specific vibrational modes, in agreement with Ref. [51].

IV. CONCLUSIONS

In summary, we have extended the MCE method to the simulation of time and frequency-resolved 4WM signals by incorporating the dynamical equations of the MCE method into the nonlinear response function formalism. The method developed here has been utilized to simulate signals of three widely used spectroscopic techniques, time and frequency-resolved fluorescence spectroscopy, transient-absorption spectroscopy, and electronic 2D spectroscopy, for a two-state, 24-vibrational-mode CI model of pyrazine. It is found that the time and frequency-resolved fluorescence spectrum provides faithful mapping of the wave-packet motions in the electronic excited states and characterizes the ultrafast population transfer from the S_2 state to the S_1 state. The transient absorption spectrum also monitors fast initial population transfer due to the SE contribution and exhibits the almost static GSB contribution which dominates at a longer delay time between pump and probe pulses. The 2D spectrum tracks the transfer of the wave packet from the upper S_2 surface to the lower S_1 surface at short population time T_w. The recurrence of 2D spectra at longer T_w is modulated by the tuning mode Q_1, which reflects the wave packet dynamics in the electronic ground state.

Integration of the trajectory-guided Gaussian basis functions with the nonlinear response function formalism proposed in this work also allows for a general theoretical framework to extend various Gaussian basis methods to the calculations of 4WM signals of molecular systems.

It is straightforward to include higher-lying excited electronic states (which are responsible for the excited state absorption) into the present methodology by propagating the system in the higher excited state manifold between τ_2 and τ_3 in Eq. (30), which is essential, for example, to understand the mechanism of singlet fission in organic crystals [56]. It is also of great interest to study finite temperature effects on the 4WM signals, using the thermo-field dynamics approach [57] or the method of Monte-Carlo importance sampling [58]. Adopting independent trajectories of the Gaussian basis functions for the MCE method proposed in Ref. [42], the present approach can also be readily extended to *ab initio* on-the-fly calculations of various 4WM spectra of polyatomic molecules [59, 60]. Work in these directions is in progress.

ACKNOWLEDGMENTS

L. P. Chen acknowledges support from the Max-Planck Gesellschaft via the MPI-PKS visitors program. K.W. Sun would like to thank the Natural Science Foundation of Zhejiang Province (Grant No. LY18A040005) for support. M.F. Gelin acknowledges support of Hangzhou Dianzi University through the startup funding. Y. Zhao would like to thank the support of the Singapore Ministry of Education Academic Research Fund Tier 1 (Grant No. RG190/18) and Tier 2 (Grant No. MOE2019-T2-1-085). D.V.S. acknowledges EPSRC (Grant No. EP/P021123/1).

V. DATA AVAILABILITY

The data that support the findings of this study are available from the corresponding author upon reasonable request.

---

[1] D. Abramavicius, B. Palmieri, D. V. Voronine, F. Šanda and S. Mukamel, Chem. Rev. **109**, 2350 (2009).

[2] S. Mukamel, *Principles of Nonlinear Optical Spectroscopy* (Oxford University Press, Oxford, 1995).

[3] L. Chen, P. Shenai, F. Zheng, A. Somoza and Y. Zhao. Molecules, 20, 15224 (2015).

[4] G. D. Scholes, G. R. Fleming, L. X. Chen, A. A. Guzik, A. Buchleitner, D. F. Coker, G. S. Engel, R. van Grondelle, A. Ishizaki, D. M. Jonas, J. S. Lundeen, J. K. McCusker, S. Mukamel, J. P. Ogilvie, A. O. Castro, M. A. Ratner, F. C. Spano, K. B. Whaley, X. Y. Zhu, Nature. **543**, 647 (2017).

[5] J. S. Cao, R. J. Cogdell, D. F. Coker, H. G. Duan, J. Hauer, U. Kleinekathöfer, T. L. C. Jansen, T. Mancăl, R. J. D. Miller, J. P. Ogilvie, V. I. Prokhorenko, T. Renger, H. S. Tan, R. Tempelaar, M. Thorwart, E. Thyrhaug, S. Westenhoff, and D. Zigmantas, Sci. Adv. **6**, 14, eaaz4888 (2020).

[6] W. Domcke, D. R. Yarkony, and H. Köppel, *Conical Intersection: Electronic structure, Dynamics and Spectroscopy* (World Scientific, Singapore, 2004).

[7] W. Domcke, D. R. Yarkony, and H. Köppel, Annu. Rev. Phys. Chem. **63**, 325 (2012).

[8] L. Valkunas, D. Abramavicius, and T. Manąl, *Molecular Excitation Dynamics and Relaxation* (Wiley-VCH, Weinheim, 2013).

[9] H. P. Breuer, F. Peetruccione. *The Theory of Open Quantum Systems* (Oxford University Press, New York, 2002).

[10] A. G. Redfield, IBM. J. Res. Dev. **1**, 19 (1957).

[11] A. Nazir, Phys. Rev. Lett. **103**, 146404 (2009).

[12] D. P. S. McCutcheon, A. Nazir. J. Chem. Phys. **135**, 114501 (2011).

[13] Y. Tanimura, J. Phys. Soc. Jpn. **75**, 082001 (2006).

[14] Y. Tanimura, J. Chem. Phys. **153**, 020901 (2020).

[15] N. Makri, D. E. Makarov, J. Chem. Phys. **102**, 4600 (1995).

[16] M. H. Beck, A. Jäckle, G. A. Worth, H. D. Meyer, Phys. Rep. **324**, 1 (2000).

[17] G. A. Worth, H. D. Meyer, H. Köppel, L. S. Cederbaum, I. Burghardt, Int. Rev. Phys. Chem. **27**, 569 (2008).

[18] H. Wang, M. Thoss. J. Chem. Phys. **119**, 1289 (2003).

[19] U. Manthe. J. Chem. Phys. **128**, 164116 (2008).

[20] B. F. E. Curchod, T. J. Martínez. Chem. Rev. **118**, 3305 (2018).

[21] M. Ben-Nun, T. J. Martínez, J. Chem. Phys. **112**, 6113 (2000).

[22] M. Ben-Nun, T. J. Martínez, Adv. Chem. Phys. **121**, 439 (2002).

[23] D. V. Shalashilin, M. S. Child, J. Chem. Phys. **113**, 10028 (2000).

[24] D. V. Shalashilin, M. S. Child, Chem. Phys. **304**, 103 (2004).

[25] D. V. Shalashilin, J. Chem. Phys. **130**, 244101 (2009).

[26] L. Chen, M. F. Gelin, D. V. Shalashilin, J. Chem. Phys. **151**, 244116 (2019)

[27] G. W. Richings, I. Polyak, K. E. Spinlove, G. A. Worth, I. Burghardt and B. Lasorne. Int. Rev. Phys. Chem. **34**, 269 (2015).

[28] A. S. Márquez, L. Chen, K. Sun, Y. Zhao, Phys. Chem. Chem. Phys. **18**, 20298 (2016)

[29] N. J. Zhou, L. P. Chen, Z. K. Huang, K. W. Sun, Y. Tanimura, and Y. Zhao, J. Phys. Chem. A **120**, 1562 (2016).

[30] Y. Fujihashi, L. Wang, and Y. Zhao, J. Chem. Phys. **147**, 234107 (2017)

[31] L. Chen, R. Borrelli, Y. Zhao, J. Phys. Chem. A. **121**, 8757 (2017).

[32] L. Chen, M. F. Gelin, W. Domcke, J. Chem. Phys. **150**, 024101 (2019).

[33] W. Hu, K.W. Sun, Q. Xu, L. Chen, and Y. Zhao, J. Chem. Phys. **153**, 174105 (2020).

[34] I. Burghardt, K. Giri and G. A. Worth, J. Chem. Phys. **129**, 174104 (2008).

[35] M. Šulc, H. Hernández, T. J. Martínez, and J. Vaníček, J. Chem. Phys. **139**, 034112 (2013).

[36] B. Mignolet, B. F. E. Curchod, T. J. Martínez, J. Chem. Phys. **145**, 191104 (2016).

[37] C. Symonds, J. Wu, M. Ronto, C. Zagoya, C. Figueira de Morisson Faria, and D. V. Shalashilin, Phys. Rev. A. **91**, 023427 (2015).

[38] T. D. Huynh, K. Sun, M. F. Gelin, and Y. Zhao. J. Chem. Phys. **139**, 104103 (2013).

[39] K. Sun, M. F. Gelin, V. Y. Chernyak, and Y. Zhao, J. Chem. Phys. **142**, 212448 (2015).

[40] D. Picconi, J. A. Cina, I. Burghardt, J. Chem. Phys. **150**, 064112 (2019).

[41] T. Begušić and J. Vaníček, J. Chem. Phys. **153**, 184110 (2020).

[42] D. V. Shalashilin, J. Chem. Phys. **132**, 244111 (2010).

[43] G. A. Worth, H. D. Meyer, and L. S. Cederbaum, J. Chem. Phys. **105**, 4412 (1996).

[44] G. A. Worth, H. D. Meyer, and L. S. Cederbaum, J. Chem. Phys. **109**, 3518 (1998).

[45] O. Bramley, C. Symonds, and D. V. Shalashilin, J. Chem. Phys. **151**, 064103 (2019).

[46] K. Sun, Z. Huang, M. F. Gelin, L. Chen, and Y. Zhao, J. Chem. Phys. **151**, 114102 (2019).

[47] M. Sala, B. Lasorne, F. Gatti, and S. Guérin, Phys. Chem. Chem. Phys. **16**, 15957 (2014).

[48] M. F. Gelin, A. V. Pisliakov, and W. Domcke, Phys. Rev. A. **65**, 062507 (2002).

[49] D. Egorova, M. F. Gelin, W. Domcke, J. Chem. Phys. **122**, 134504 (2005).

[50] L. Chen, M. F. Gelin, Y. Zhao, and W. Domcke, J. Phys. Chem. Lett. **10**, 5873 (2019).

[51] K. Sun, W. Xie, L. Chen, W. Domcke, and M. F. Gelin, J. Chem. Phys. **153**, 174111 (2020).

[52] E. Palacino-González, M. F. Gelin, and W. Domcke, J. Chem. Phys. **150**, 204102 (2019).

[53] J. Krčmář, M. F. Gelin, D. Egorova, and W. Domcke, J. Phys. B: At. Mol. Opt. Phys. **47**, 124019 (2014).

[54] J. Krčmář, M. F. Gelin, and W. Domcke, J. Chem. Phys. **143**, 074308 (2015).

[55] M. Sala and D. Egorova, Chem. Phys. **481**, 206 (2016).

[56] K. Miyata, Y. Kurashige, K. Watanabe, T. Sugimoto, S. Takahashi, S. Tanaka, J. Takeya, T. Yanai, and Y. Matsumoto, Nat. Chem. **9**, 983 (2017).

[57] L. Chen and Y. Zhao, J. Chem. Phys. **147**, 214102 (2017).

[58] L. Wang, Y. Fujihashi, L. Chen, and Y. Zhao, J. Chem. Phys. **146**, 124127 (2017).

[59] D. Makhov, W. J. Glover, T. J. Martínez, and D. V. Shalashilin, J. Chem. Phys. **141**, 054110 (2014).

[60] D. Makhov, C. Symonds, S. F. Alberti, and D. V. Shalashilin, Chem. Phys. **493**, 200 (2017).